Monthly Notices
of the
ROYAL ASTRONOMICAL SOCIETY

MNRAS **493,** 4045–4057 (2020)
Advance Access publication 2020 February 21

doi:10.1093/mnras/staa518

The ASAS-SN catalogue of variable stars – VII. Contact binaries are different above and below the Kraft break

T. Jayasinghe [1,2]★ K. Z. Stanek,[1,2] C. S. Kochanek,[1,2] B. J. Shappee,[3] M. H. Pinsonneault,[1] T. W.-S. Holoien [4], Todd A. Thompson,[1,2,5] J. L. Prieto,[6,7] M. Pawlak,[8] O. Pejcha [8], G. Pojmanski,[9] S. Otero,[10] N. Hurst[11] and D. Will[1,11]

[1]*Department of Astronomy, The Ohio State University, 140 West 18th Avenue, Columbus, OH 43210, USA*
[2]*Center for Cosmology and Astroparticle Physics, The Ohio State University, 191 W. Woodruff Avenue, Columbus, OH 43210, USA*
[3]*Institute for Astronomy, University of Hawaii, 2680 Woodlawn Drive, Honolulu, HI 96822, USA*
[4]*Carnegie Observatories, 813 Santa Barbara Street, Pasadena, CA 91101, USA*
[5]*Institute for Advanced Study, Princeton, NJ 08540, USA*
[6]*Núcleo de Astronomía de la Facultad de Ingeniería y Ciencias, Universidad Diego Portales, Av. Ejército 441, Santiago, Chile*
[7]*Millennium Institute of Astrophysics, Santiago, Chile*
[8]*Institute of Theoretical Physics, Faculty of Mathematics and Physics, Charles University, Prague, Czech Republic*
[9]*Warsaw University Observatory, Al Ujazdowskie 4, PL-00-478 Warsaw, Poland*
[10]*The American Association of Variable Star Observers, 49 Bay State Road, Cambridge, MA 02138, USA*
[11]*ASC Technology Services, 433 Mendenhall Laboratory, 125 South Oval Mall, Columbus, OH 43210, USA*

Accepted 2020 February 18. Received 2020 February 18; in original form 2019 November 25

ABSTRACT

We characterize ∼71 200 W Ursae Majoris (UMa) type (EW) contact binaries, including ∼12 600 new discoveries, using All-Sky Automated Survey for SuperNovae (ASAN-SN) *V*-band all-sky light curves along with archival data from *Gaia*, 2MASS, AllWISE, LAMOST, GALAH, RAVE, and APOGEE. There is a clean break in the EW period–luminosity relation at $\log(P/\mathrm{d}) \simeq -0.30$, separating the longer period, early-type EW binaries from the shorter period, late-type systems. The two populations are even more cleanly separated in the space of period and effective temperature, by $T_{\rm eff} = 6710\,\mathrm{K} - 1760\,\mathrm{K}\,\log(P/0.5\,\mathrm{d})$. Early-type and late-type EW binaries follow opposite trends in $T_{\rm eff}$ with orbital period. For longer periods, early-type EW binaries are cooler, while late-type systems are hotter. We derive period–luminosity relationships in the W_{JK}, V, *Gaia* DR2 G, J, H, $K_{\rm s}$, and W_1 bands for the late-type and early-type EW binaries separated by both period and effective temperature, and by period alone. The dichotomy of contact binaries is almost certainly related to the Kraft break and the related changes in envelope structure, winds, and angular momentum loss.

Key words: catalogues – surveys – binaries: eclipsing.

1 INTRODUCTION

Contact binaries are close binary systems whose components fill their Roche lobes. The most abundant are the W Ursae Majoris (W UMa) variables that are characterized by having nearly equal primary and secondary eclipse depths and orbital periods of ∼0.2–1 d. Given that both stars overflow their Roche lobes, the orbital periods of W UMa variables are closely related to the mean stellar densities (Eggleton 1983). As a result, these contact binaries follow a period–luminosity relationship (PLR), which can yield distances accurate to 10 per cent (Rucinski 1994; Chen, de Grijs & Deng 2016; Chen et al. 2018). W UMa variables show little colour variability and similar eclipse depths, so the component stars have similar effective temperatures and are in thermal contact (Webbink 2003). In most variable star catalogues, W UMa variables are assigned the GCVS/VSX (Watson, Henden & Price 2006; Samus et al. 2017) classification of 'EW'.

W UMa variables are abundant in the Galaxy, and the advent of wide-field surveys, such as the All-Sky Automated Survey (ASAS; Pojmanski 2002), the Optical Gravitational Lensing Experiment (OGLE; Udalski 2003), the Northern Sky Variability Survey (NSVS; Woźniak et al. 2004), MACHO (Alcock et al. 1997), EROS (Derue et al. 2002), the Catalina Real-Time Transient Survey (CRTS; Drake et al. 2014), and the Asteroid Terrestrial-impact Last Alert System (ATLAS; Heinze et al. 2018; Tonry et al. 2018a), have yielded $\gtrsim 10^5$ such variables. Using the ASAS catalogue, Rucinski (2006) estimated an abundance relative to FGK stars of 0.2 per cent.

★ E-mail: jayasinghearachchilage.1@osu.edu

Given their high occurrence rates, they can also be used to study Galactic structure (Rucinski 1997).

Contact binaries play a significant role in stellar evolution and, maybe, the progenitors for objects such as blue stragglers (Andronov, Pinsonneault & Terndrup 2006; Chen & Han 2009) and Oe/Be stars (Eggleton 2010; de Mink et al. 2013). In one case, a contact binary was observed to evolve into a stellar merger (Tylenda et al. 2011). Thus, the study of the formation and evolution of contact binaries will improve our understanding of binary mergers and stellar evolution.

The detached-binary channel is considered to be crucial for the formation of contact binaries (Rucinski 1986; Li et al. 2007; Jiang, Han & Li 2014). In this channel, a close detached binary evolves to Roche lobe overflow and then to contact either through the evolutionary expansion of the components (Webbink 1976) or through angular momentum loss by magnetic braking (Vilhu 1982). Studies of chromospherically active binaries have shown that they are losing angular momentum and evolving towards shorter orbital periods, making them good candidates for the progenitors of contact binaries (Eker et al. 2006). Paczyński et al. (2006) studied the eclipsing binaries (EBs) in the ASAS catalogue and noted a deficiency of close detached binaries with periods $P < 1$ d compared to the number needed to produce the observed number of contact binaries. It seems likely that many contact binaries form in triple systems, where the Kozai–Lidov mechanism (Kozai 1962; Lidov 1962) drives the evolution towards becoming contact binaries (Eggleton & Kiseleva-Eggleton 2001). The formation time-scale of contact binaries from a single starbust in the detached-binary channel has a large dynamic range (∼1 Myr–15 Gyr, Jiang et al. 2014), which can explain the existence of very young contact binaries (<10 Myr) (Van Eyken et al. 2011).

W UMa contact binaries are observationally classified into A-type and W-type systems. The primary eclipse in the A-type systems corresponds to the transit of the secondary across the primary, whereas W-type systems are those whose secondaries are occulted by the primary. The sub-types also have different spectral types. A-type systems have A–F spectra and W-type systems have G–K spectra (Webbink 2003). Thus, the two sub-types appear to be separated in temperature, with A-type systems having temperatures $\gtrsim$6000 K (Rucinski 1974). The massive component of an A-type system is hotter than the less massive component and the opposite is true for W-type systems (Binnendijk 1970; Yildiz & Doğan 2013). The formation mechanism of A-type contact binaries in the pre-contact phase is dominated by the nuclear evolution of the more massive component ($1.8 < M < 2.7\,M_{\odot}$) and the angular momentum evolution of the less massive component ($0.2 < M < 1.5\,M_{\odot}$) (Yildiz 2014). The pre-contact phases for the A-type systems typically end as the primary begins to evolve off the main sequence. In the W-type systems, both components undergo an efficient angular momentum loss, and in most cases, the angular momentum evolution is so rapid that the binary evolves into contact before the primary leaves the main sequence (Yildiz 2014). In this paper, we will refer to the A-type systems as early-type EW binaries and the W-type systems as late-type EW binaries. The early/late types are related to the W/A sub-types, but the classifications are not completely identical.

Main-sequence stars follow two distinct rotational regimes that are determined by how efficiently the stars lose angular momentum. Stars cooler than $T_{\rm eff} \lesssim 6200$ K are slow rotators (Van Saders & Pinsonneault 2013). These stars have thick convective envelopes, and rapidly lose their angular momentum due to magnetized winds. Hot stars with $T_{\rm eff} \gtrsim 6700$ K rotate rapidly (Royer, Zorec & Gómez 2007) because they do not have thick convective envelopes, and angular momentum loss through magnetized winds becomes very inefficient. The transition from the slowly rotating main-sequence stars to the rapidly rotating main-sequence stars occurs at $\sim$1.3 $M_{\odot}$ (early F spectral types) and is known as the Kraft break (Kraft 1967). The differences in angular momentum loss above and below the Kraft break presumably drive the evolutionary difference between the early- and late-type binaries.

In a series of papers, Jayasinghe et al. (2018, 2019b,c,d,in preparation), we have been systematically identifying and classifying variables using data from the All-Sky Automated Survey for SuperNovae (ASAS-SN; Shappee et al. 2014; Kochanek et al. 2017). We have thus far discovered ∼220 000 new variables and homogeneously classified both the new and previously known variables in the sample (Jayasinghe et al. 2019a). Here, we analyse an all-sky catalogue of 71 242 W UMa (EW) contact binaries in the ASAS-SN *V*-band data. In Section 2, we summarize the ASAS-SN catalogue of EW binaries and the cross-matching to the external photometric and spectroscopic catalogue. We analyse the sample of EW binaries with spectroscopic cross-matches and compare early-type and late-type systems in Section 3. We derive period–luminosity relationships (PLRs) for these two sub-types in Section 4. The *V*-band light curves and other variability and photometric information for all of the ∼71 200 sources studied in this work are available online at the ASAS-SN variable stars data base (https://asas-sn.osu.edu/variables).

2 THE ASAS-SN CATALOGUE OF CONTACT BINARIES

In this work, we selected 71 242 W UMa-type contact binary stars (EW) identified during our systematic search for variables, including new EW binaries in the Northern hemisphere and regions of the southern Galactic plane that were missed in the previous survey papers (Jayasinghe et al., in preparation). Out of the 71 242 EW binaries in this catalogue, 12 584 (∼18 per cent) are new ASAS-SN discoveries. The ASAS-SN *V*-band observations used in this work were made by the 'Brutus' (Haleakala, Hawaii) and 'Cassius' (CTIO, Chile) quadruple telescopes between 2013 and 2018. Each ASAS-SN *V*-band field is observed to a depth of $V \lesssim 17$ mag. The field of view of an ASAS-SN camera is 4.5 deg^2, the pixel scale is 8.0 arcsec, and the full width at half-maximum is typically ∼2 pixels. ASAS-SN saturates at ∼10–11 mag, but we attempt to correct the light curves of saturated sources for bleed trails (see Kochanek et al. 2017). The *V*-band light curves were extracted as described in Jayasinghe et al. (2018) using image subtraction (Alard & Lupton 1998; Alard 2000) and aperture photometry on the subtracted images with a 2-pixel-radius aperture. The APASS catalogue (Henden et al. 2015) and the ATLAS All-Sky Stellar Reference catalogue (Tonry et al. 2018b) were used for calibration. We corrected the zero-point offsets between the different cameras, as described in Jayasinghe et al. (2018). The photometric errors were re-calculated, as described in Jayasinghe et al. (2019b).

Variable sources were identified and subsequently classified using two independent random forest classifiers plus a series of quality checks, as described in Jayasinghe et al. (2019a,d). We used the ASTROPY implementation of the Generalized Lomb–Scargle (GLS; Scargle 1982; Zechmeister & Kürster 2009) periodogram and the `astrobase` implementation (Bhatti et al. 2018) of the Box Least Squares (BLS; Kovács, Zucker & Mazeh 2002) periodogram, which improves the completeness for EBs, to search for periodicity over the range $0.05 \leq P \leq 1000$ d. We classified the EBs into the

GCVS/VSX photometric (sub-)classes, EW, EB, and EA. EW (W UMa) binaries have light curves with minima of similar depths, whereas EB (β-Lyrae) binaries tend to have minima of significantly different depths. The ratio of eclipse depths (D_s/D_p) for most contact binaries is $D_s/D_p > 0.8$, whereas most semi-detached systems have eclipses of different depths with $D_s/D_p < 0.8$ (Paczyński et al. 2006; Jayasinghe et al. 2019a). Most contact binaries are in thermal contact, but Paczyński et al. (2006) also noted systems with unequal minima, implying that some contact binaries are not in thermal contact, as was predicted by models of thermal relaxation oscillations (see e.g. Flannery 1976; Lucy 1976; Yakut & Eggleton 2005). Both the EW (contact) and EB (contact/semi-detached) binaries transition smoothly from the eclipse to the out-of-eclipse state. EA (Algol) binaries are detached systems where the exact onset and end of the eclipses are easily defined. These detached systems may or may not have a secondary minimum.

We cross-matched the EW binaries with *Gaia* DR2 (Gaia Collaboration et al. 2018a) using a matching radius of 5.0 arcsec. The sources were assigned distance estimates from the *Gaia* DR2 probabilistic distance estimates (Bailer-Jones et al. 2018) by cross-matching based on the *Gaia* DR2 `source_id`. A large majority of these sources (∼86.8 per cent) had distance estimates from *Gaia* DR2. We also cross-matched these sources to the 2MASS (Skrutskie et al. 2006) and AllWISE (Wright et al. 2010; Cutri et al. 2013) catalogue using a matching radius of 10.0 arcsec. We used TOPCAT (Taylor 2005) for this process. Following the cross-matching process, we calculated the absolute, reddening-free Wesenheit magnitude (Madore 1982; Lebzelter et al. 2018) for each source as

$$W_{JK} = M_{K_s} - 0.686(J - K_s)\,. \quad (1)$$

For each source, we also calculate the total line-of-sight Galactic reddening $E(B - V)$ from the recalibrated 'SFD' dust maps (Schlegel, Finkbeiner & Davis 1998; Schlafly & Finkbeiner 2011).

We cross-matched our sample with the APOGEE DR15 catalogue (Holtzman et al. 2015; Majewski et al. 2017), RAVE-on catalogue (Casey et al. 2017), LAMOST DR5 v4 catalogue (Cui et al. 2012), and GALAH DR2 catalogue (De Silva et al. 2015; Buder et al. 2018) using a matching radius of 5.0 arcsec. We identified 7169 matches to the EW binaries from the LAMOST (94.0 per cent), GALAH (3.8 per cent), RAVE (2.1 per cent), and APOGEE (0.1 per cent) spectroscopic surveys.

The median V-band magnitude of the EW binary sample is $V \sim 14.7$ mag. Classification probabilities of Prob > 0.9 are considered very reliable, and ∼93.4 per cent of our sample of contact binaries have Prob > 0.9. There are 21 837 sources within 1 kpc, but a considerable fraction (∼69 per cent) of the sources with *Gaia* DR2 distances are located farther away. A large fraction have useful parallaxes, as ∼69 per cent (∼58 per cent) of the sources have `parallax/parallax_error` >5 (>10). The median line-of-sight extinction to the EW binaries is $A_V \sim 0.36$ mag, assuming $R_V = 3.1$ dust (Cardelli, Clayton & Mathis 1989). The sky distribution of the EW binaries in ASAS-SN, coloured by their period, is shown in Fig. 1.

We present the ASAS-SN light curves for 10 late-type and 10 early-type contact binaries to illustrate the light-curve morphologies of these systems. The phased ASAS-SN V- and g-band light curves are shown in Figs 2 (late-type EW) and 3 (early-type EW). The ratio of eclipse depths is similar for both the late-type and early-type binaries. We do not see substantial differences in the morphologies of the light curves between early-type and late-type contact binaries. The variations in the depths of the minima are generally only a few per cent (Webbink 2003), making it challenging to distinguish the early- and late-type systems using the ASAS-SN light curves.

The period distribution of the EW binaries is shown in Fig. 4. The EW binaries have a bimodal orbital period distribution, with the late-type systems [canonically defined as those with $\log(P/\mathrm{d}) < -0.25$] having a median period of $\log(P/\mathrm{d}) \sim -0.4$, and the early-type systems having a median period of $\log(P/\mathrm{d}) \sim -0.15$. Most sources with periods $P > 1$ d are likely β-Lyrae EBs, with nearly equal minima that are misclassified as contact (EW) binaries. We will discuss the differences between early-type and late-type contact binaries in Section 3 and derive PLRs for these two sub-types in Section 4.

3 EARLY-TYPE VERSUS LATE-TYPE W UMA CONTACT BINARIES

In previous studies, early-type and late-type EW binaries are usually separated on the basis of their period, with the early-type systems defined to have orbital periods $\log(P/\mathrm{d}) > -0.25$ (e.g. Chen et al. 2018). It is also known that the early-type systems are fewer in number than the late-type systems (Pawlak 2016). Fig. 5 shows the Wesenheit W_{JK} PLR diagram for the EW binaries with classification probabilities of Prob > 0.9, $A_V < 1$ mag, and `parallax/parallax_error` >10. In the sample of ASAS-SN contact binaries, we immediately see that the slope of the late-type PLR is steeper than that of the early-type systems. Pawlak (2016) studied a sample of early-type contact binaries in the Large Magellanic Cloud discovered by the OGLE survey (Graczyk et al. 2011; Pawlak et al. 2016) and noted that the PLRs for contact binaries are best described by two separate relations for the late-type and early-type systems. He found a shallower slope for the early-type contact binaries when compared to the late-type PLR. The PLRs for late-type EW binaries have been extensively studied (Rucinski 1994; Chen et al. 2016, 2018).

While the traditional period for separating early- and late-type EW systems is at $\log(P/\mathrm{d}) = -0.25$, the clear minimum in the period distribution (Fig. 4) suggests that $\log(P/\mathrm{d}) = -0.30$ is a better choice. In practice, the two classes have some period overlap with early-type systems having periods as short as $\log(P/\mathrm{d}) = -0.40$ and late-type systems having periods as long as $\log(P/\mathrm{d}) = -0.25$. Fig. 5 shows the distribution of the systems in period and W_{JK}, and we see a clear break in the slope at a period of $\log(P/\mathrm{d}) \sim -0.30$. We will fit models for the PLR in Section 4 after improving the separation between the early-type and late-type systems.

Jiang et al. (2014) found that the upper limit of the initial orbital period for binaries that come into contact (∼3–4.2 d) is significantly longer than the upper limit of the observed EW period distribution (∼1–2 d). Thus, the orbital period distribution for the EW binaries reflects significant orbital shrinkage compared to a zero-age binary population. This implies that the physics of the merger process must be responsible for shaping the observed PLRs of the early-type and late-type systems. A successful theory has to consider the evolution from a detached system to a contact system.

Fig. 6 shows the distributions in effective temperature $T_{\rm eff}$, surface gravity $\log(g)$, and metallicity [Fe/H] for the early-type and late-type contact binaries with Prob > 0.90 in the APOGEE, LAMOST, GALAH, and RAVE surveys. The distributions of the late-type ($N = 5248$) and early-type ($N = 888$) contact binaries in $\log(g)$ and [Fe/H] are similar. There appears to be an excess of early-type binaries with [Fe/H] < −0.8. However, upon further inspection, we find that a substantial fraction of these low-metallicity sources are actually misclassified overtone RR Lyrae (RRc) variables that

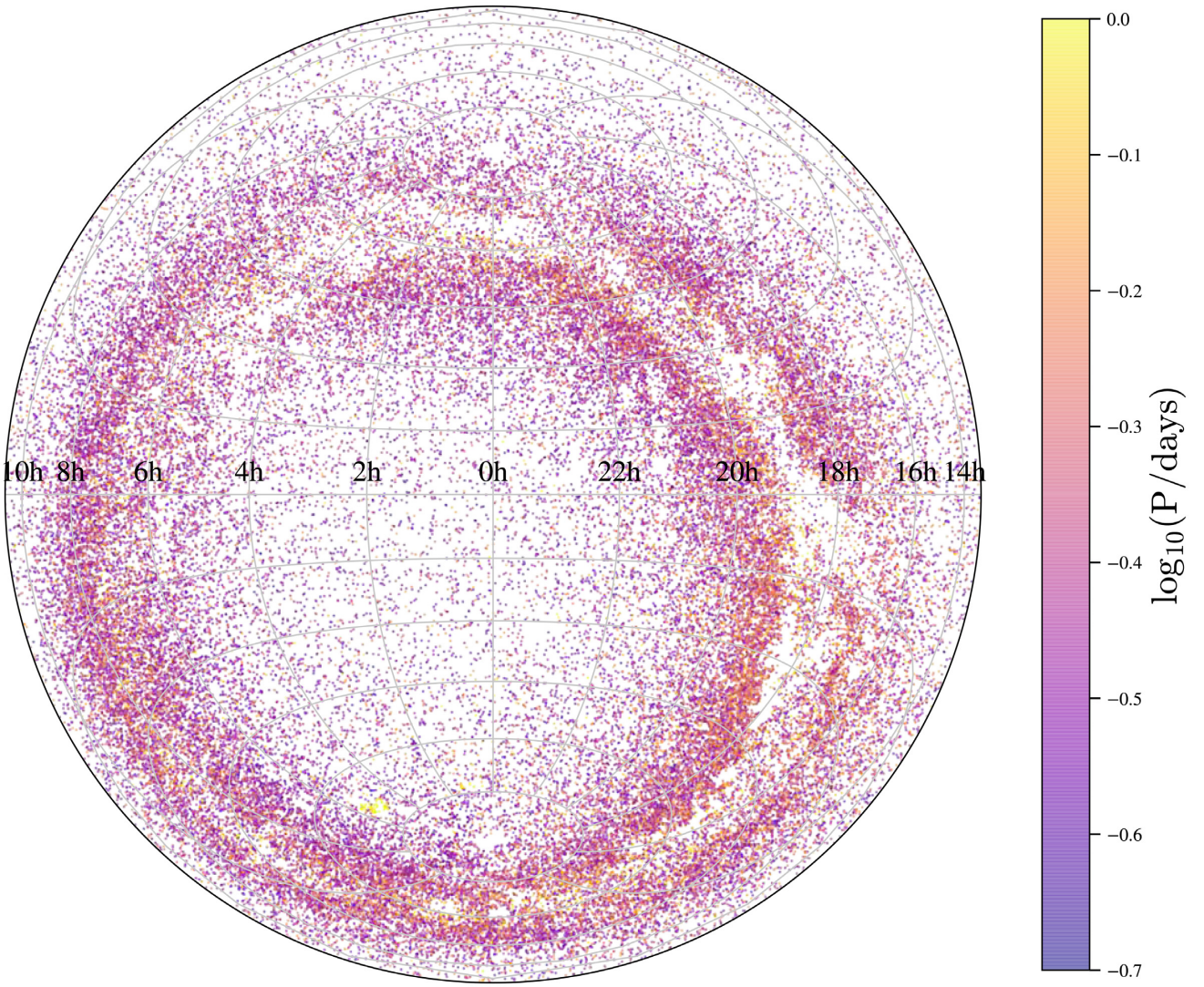

Figure 1. Projected distribution of the ∼ 71 200 EW binaries in equatorial coordinates (Lambert projection). The points are coloured by period.

were assigned twice their true pulsational period in the ASAS-SN pipeline. RRc variables are sometimes confused with EW variables because of their symmetric light-curve morphologies. We discard early-type binaries with [Fe/H] < -0.8 to minimize contamination.

The temperature distributions are, of course, quite different, but the separation of the two populations is very striking in the space of $\log(P/\mathrm{d})$ and $T_{\rm eff}$, as shown in Fig. 7. The increase in temperature with period is well known for the late-type systems, going back to the observation that longer period systems are bluer. The trend reverses for the late-type systems, which has not previously been observed. Qian et al. (2017) noted a trend but dismissed it as scatter. Still more striking is that there is a clean break between the two populations, which we can empirically model as

$$T_{\rm eff} = 6710\,\mathrm{K} - 1760\,\mathrm{K}\,\log(P/0.5\,\mathrm{d})\,. \quad (2)$$

The traditional cut-in period is an approximation to the actual separation of the two populations, but a period separation of $\log(P/\mathrm{d}) = -0.30$ at the minimum of the period distribution is a better 'average' choice than the traditional $\log(P/\mathrm{d}) = -0.25$. We use equation (2) to separate the two populations in the spectroscopic sample.

The existence of the Kraft break (Kraft 1967) implies substantial changes in the envelope structure, winds, and angular momentum loss for stars on the main sequence. Stars above the Kraft break are hotter and rotate more rapidly than those below the Kraft break. The transition from slow to fast rotation occurs over the temperature range 6200–6700 K, and it cannot be a coincidence that the split between early- and late-type contact binaries occurs at a similar temperature. Formation models for these systems generally invoke changes in the efficiency of angular momentum loss on the main sequence (Yildiz 2014), which is exactly the physics leading to the Kraft break. The remarkable feature of Fig. 7 is the existence of a clear gap between early- and late type systems, which seems not to be predicted in any models.

If we separate the systems using equation (2), we find period–temperature relations of

$$T_{\rm eff}\ (\mathrm{LT}) = 6598(\pm23)\,\mathrm{K} + 5260(\pm116)\,\mathrm{K}\,\log_{10}(P/0.5\,\mathrm{d}), \quad (3)$$

for the late-type systems and

$$T_{\rm eff}\ (\mathrm{ET}) = 7041(\pm28)\,\mathrm{K} - 843(\pm164)\,\mathrm{K}\,\log_{10}(P/0.5\,\mathrm{d}), \quad (4)$$

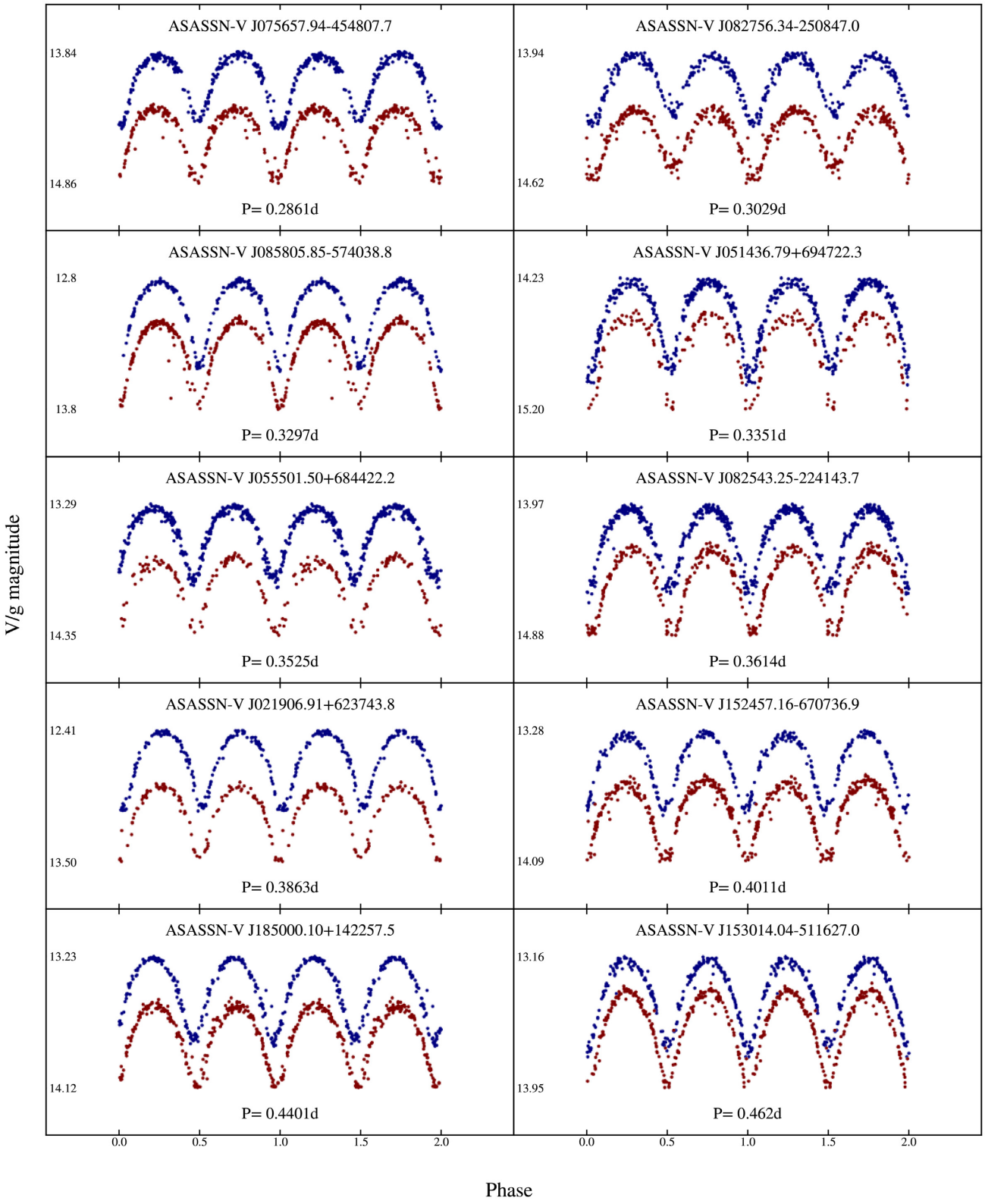

Figure 2. Phased ASAS-SN light curves for 10 late-type EW binaries. The light curves are scaled by their minimum and maximum *V*/*g*-band magnitudes. The blue (red) points are for the *g*(*V*)-band data.

for the early-type systems. Both these relationships have large scatter ($\sigma \gtrsim 300$ K); however, it is clear that the slopes are not only very different but also reverse in sign (Fig. 8). This can also be seen in the period–colour distributions shown in Fig. 9. Historically, the period–colour relation of late-type systems have been well characterized (Eggen 1961, 1967). Here we see that the early-type systems become redder (cooler) with increasing orbital period, which is the reverse of the well-known correlations for the late-type systems.

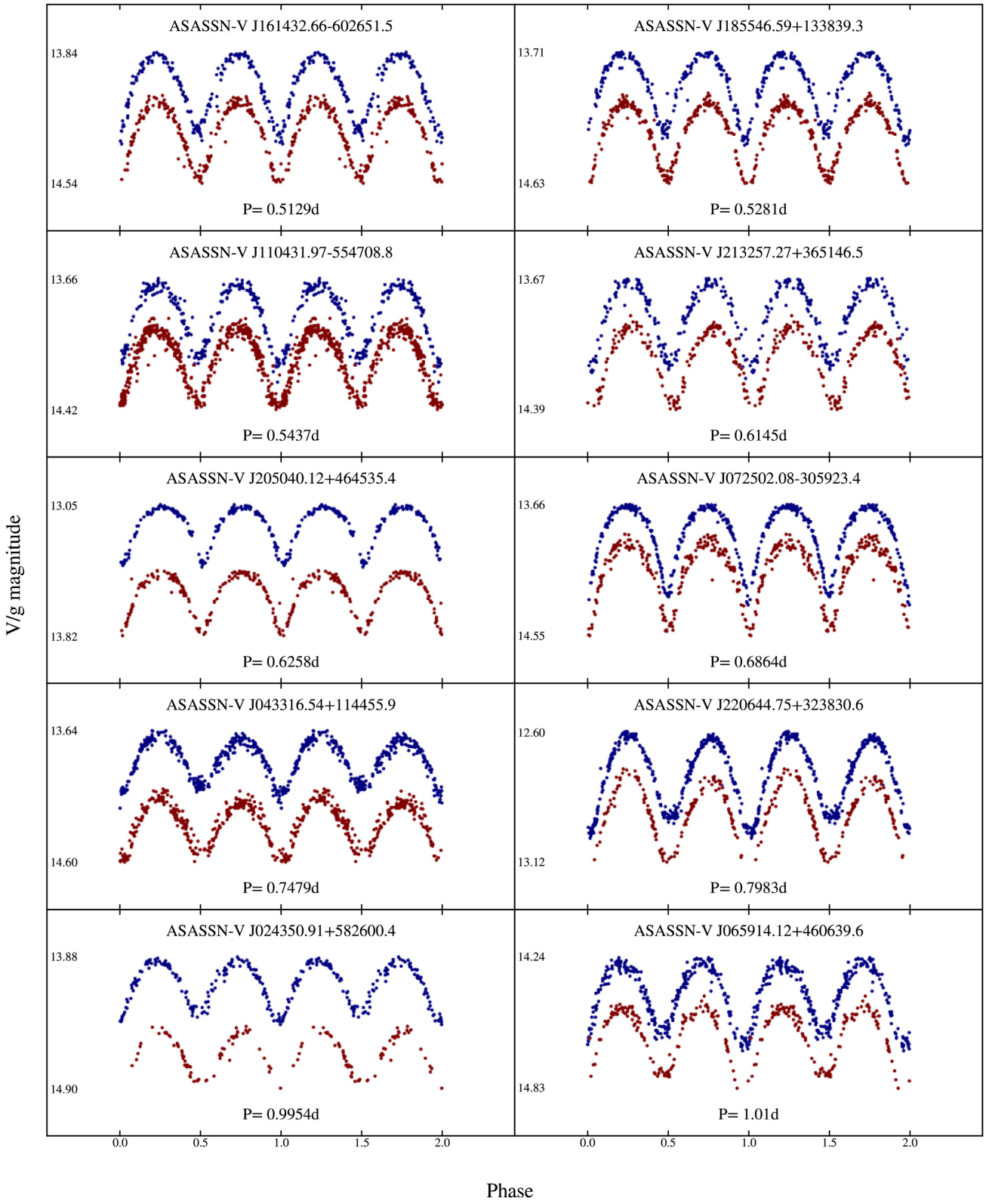

Figure 3. Phased ASAS-SN light curves for 10 early-type EW binaries. The format is the same as Fig. 2.

Fig. 10 shows the distribution of the spectroscopically classified systems in $\log(g)$ and [Fe/H] versus temperature. For comparison, we show MESA Isochrones and Stellar Tracks isochrones (MIST; Choi et al. 2016; Dotter 2016) for single stars with [Fe/H] $= -0.25$ at 1, 2, 3, 5, and 10 Gyr. The metallicity was chosen to match the median of the early-type systems. While using single star isochrones to interpret binaries combined with spectroscopic data models designed for single stars is risky, it is worth remembering that these

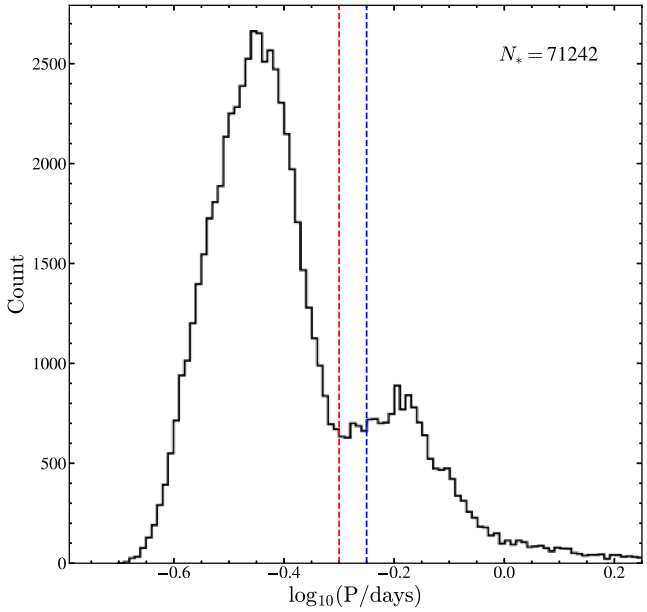

Figure 4. The distribution of orbital periods for the ∼ 71 200 EW binaries. The usual period cut separating early-type and late-type systems of $\log(P/\mathrm{d}) = -0.25$ is shown as a dashed blue line. A revised period cut of $\log(P/\mathrm{d}) = -0.30$ based on the period distribution of the EW binaries in ASAS-SN is shown as a dashed red line.

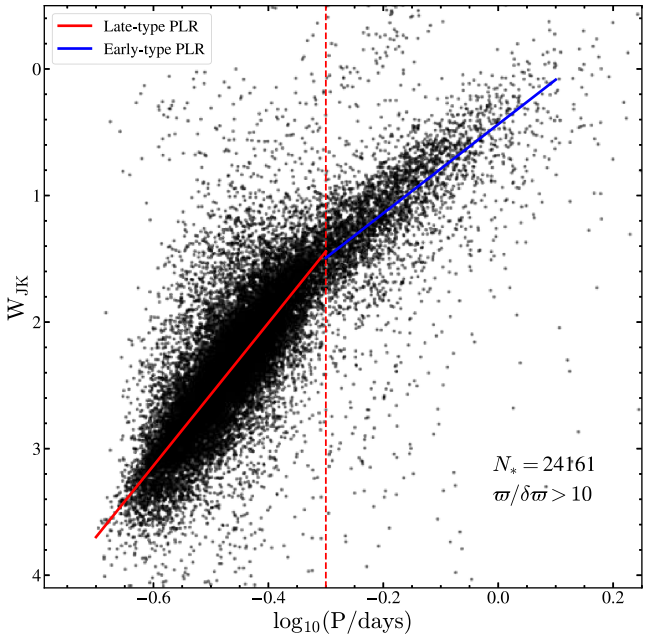

Figure 5. The Wesenheit W_{JK} PLR diagram for the EW stars with Prob > 0.90, $A_V < 1$ mag, and parallaxes better than 10 per cent. The fitted PLRs for the late-type and early-type contact binaries are shown as red and blue lines, respectively.

systems basically have a single temperature. The most interesting feature of Fig. 10 is probably that the systems have significantly lower $\log(g)$ than expected for main-sequence stars. For the higher mass systems, this could be due to evolution, but the effect is present even for the lower mass systems that should not have had time to evolve. The offset seems to be largest near the break temperature and smallest at higher and lower temperatures. El-Badry et al. (2018) did find that $\log(g)$ was moderately underestimated in fits of single-star models to semi-empirical binary models, and we also find that detached binaries have similar offsets in $\log(g)$. Non-variable single stars in the LAMOST survey have $\log(g)$ values consistent with models of main-sequence stars, so either the $\log(g)$ values are more biased than expected from El-Badry et al. (2018) or there is a genuine difference. There also appears to be a weak trend of the systems having higher metallicities at lower temperatures.

Fig. 11 shows the early-type and late-type contact binaries with $A_V < 1$ mag and parallaxes better than 10 per cent in a *Gaia* DR2 colour–magnitude diagram (CMD) after correcting for interstellar extinction. A sample of nearby sources with good parallaxes and photometry is shown in the background. The isochrones do not track the main sequence of the nearby stars as these have near-solar metallicities, while the isochrones are for a lower metallicity ([Fe/H] = −0.25). As expected, both groups of contact binaries are more luminous than stars on the main sequence and the early-type systems are more luminous than the late-type systems due to their higher masses.

Fig. 12 shows the same early-type and late-type sources in Fig. 11, coloured by $\log(T_{\rm eff})$. The average temperature of the early-type binaries drops with the perpendicular distance from the main sequence; thus, early-type binaries are cooler if they are farther from the main sequence. The late-type binaries do not show a similar gradient in temperature with the perpendicular distance from the main sequence. The temperature simply increases with luminosity.

We use the empirical orbital period–mass relations derived in Gazeas & Stępień (2008) to derive estimates of the primary and secondary masses for the contact binaries with spectroscopic data. The masses derived from these relations have uncertainties of ∼15 per cent. The 1–99 per cent quantile ranges of primary masses of the early-type and late-type systems were 1.27–3.29 and 0.88–1.67 $\mathrm{M}_\odot$, respectively, whereas the distributions of secondary masses were 0.39–0.61 and 0.33–0.44 $\mathrm{M}_\odot$, respectively. The total masses of the early-type and late-type systems were 1.66–3.90 and 1.20–2.12 $\mathrm{M}_\odot$, respectively. The total masses of the W UMa binaries grow with the orbital period. These mass estimates are comparable to the theoretical estimates from Yildiz (2014). The median masses of the primaries for the early-type and late-type systems are 1.8 and 1.2 $\mathrm{M}_\odot$, respectively. The masses of the primaries in the early-type (late-type) systems are consistent with their being above (below) the Kraft break. Simple main-sequence lifetime arguments for the primaries of the early-type stars suggest that most of the sample should evolve off the main sequence at ∼2 Gyr, whereas the majority of the primaries of the late-type stars should evolve off the main sequence at ∼6 Gyr. This agrees with Figs 11 and 12, where the early-type systems seem to be more evolved.

4 PERIOD–LUMINOSITY RELATIONSHIPS

PLRs exist only for late-type EW systems and are based on small samples (Rucinski 1994; Chen et al. 2018). Here we derive PLRs using much larger samples and for both early- and late-type systems. We derive PLRs as

$$M_\lambda = A \log_{10}(P/0.5\,\mathrm{d}) + B, \quad (5)$$

following the procedure in Jayasinghe et al. (in preparation). We corrected for interstellar extinction with the SFD estimate. We include systems with `parallax/parallax_error` >20, Prob > 0.98, and $A_V < 1$ mag to reduce the uncertainty in the absolute magnitudes. We made an initial fit to each band, after

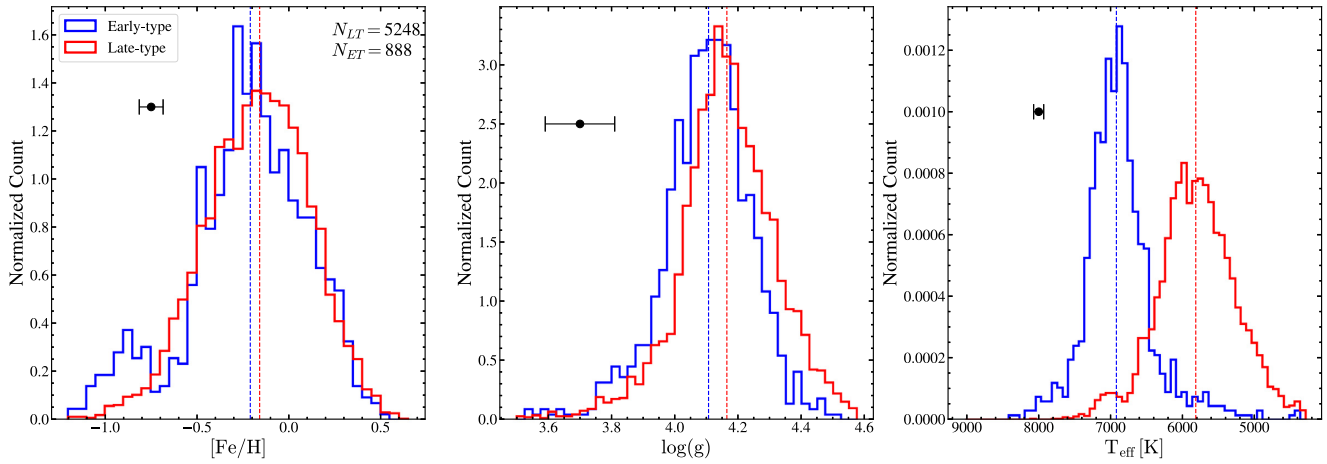

Figure 6. Distributions of the late-type (red) and early-type (blue) EW contact binaries with Prob > 0.9 in [Fe/H], log(g), and $T_{\rm eff}$. The median value for each parameter is illustrated with a dashed line. The average uncertainty for each parameter is shown in black. The excess of early-type binaries with [Fe/H] < -0.8 is due to misclassified RRc variables.

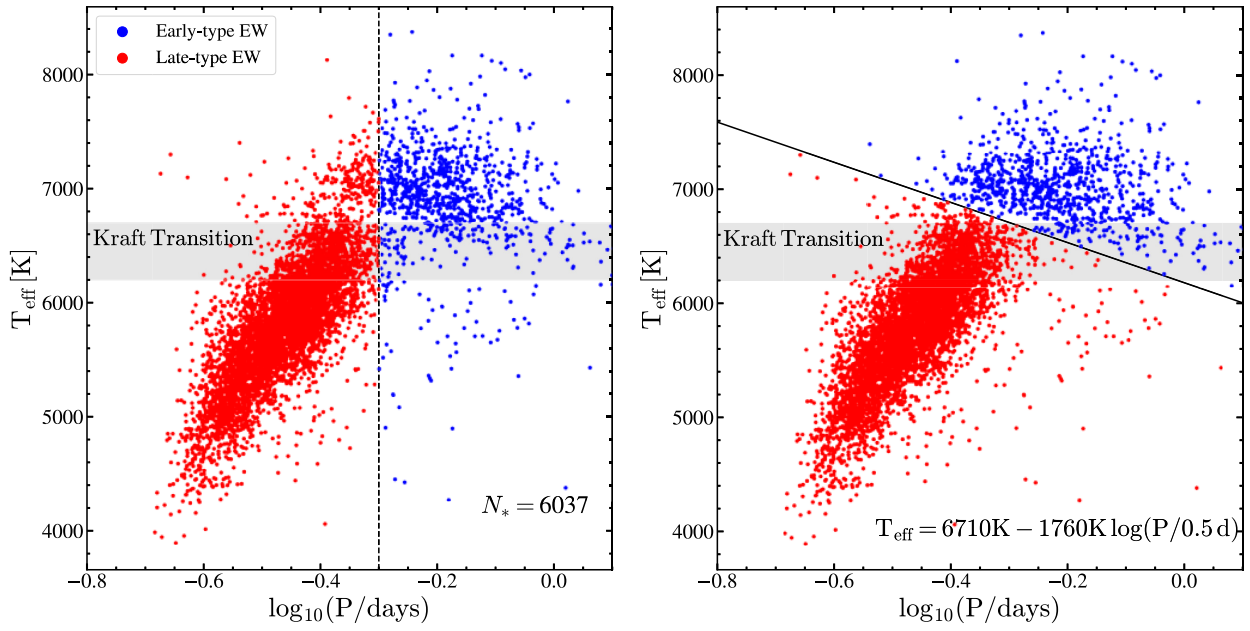

Figure 7. $T_{\rm eff}$ versus log(P/d) for late-type (red) and early-type (blue) EW binaries separated by period (left-hand panel) and a discriminant in $T_{\rm eff}$- log(P/d) (right-hand panel). The Kraft transition from slow to fast rotation occurs over the temperature range 6200–6700 K and is shaded in grey.

which we removed outliers from the PLR fit by calculating the distance from the initial fit:

$$r = \sqrt{(\Delta \log_{10} P)^2 + (\Delta M_\lambda)^2},$$

where

$$\Delta \log_{10}(P) = \log_{10}(P_{\rm fit}/P_{\rm obs}),$$

and

$$\Delta M_\lambda = M_{\lambda,{\rm fit}} - M_{\lambda,{\rm obs}}.$$

Sources that deviated from this fit by $>2\sigma_r$ were removed. After removing these outliers, the parameters from the trial fit were then used to initialize a Markov chain Monte Carlo (MCMC) sampler with 200 walkers, which were run for 20 000 iterations using the MCMC implementation `emcee` (Foreman-Mackey et al. 2013). The errors in the PLR parameters were derived from the MCMC chains. Since we are using photometry obtained at random phases, these PLRs essentially correspond to the PLRs for the mean magnitudes of the binaries. However, they will have an additional scatter of ∼0.05 mag because they are not individually averaged (or peak) magnitudes for each binary (Chen et al. 2018). For the early-type binaries, we use only the spectroscopic sample to avoid contamination by both late-type binaries and RRc variables, while for the late-type binaries, we augment the sample by including sources with log(P/d) < -0.4, where there is no confusion between late-type and early-type contact binaries (Fig. 7).

Given that most EW binaries do not have spectroscopic data to separate early-type and late-type systems based on equation (2), we also derive PLRs for early-type and late-type systems separated by period. Fig. 13 shows the period distribution of the early-type

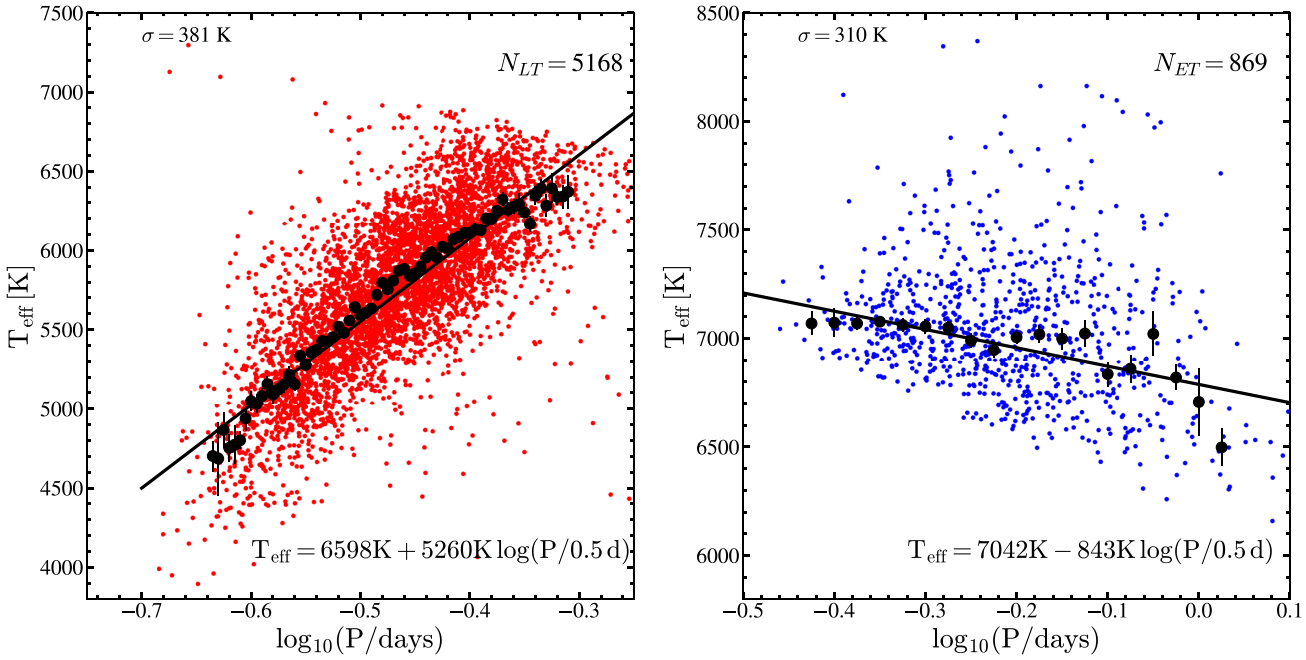

Figure 8. $T_{\rm eff}$ versus $\log(P/d)$ for the late-type (left) and early-type (right) EW binaries. Linear fits to the binned data are shown in black.

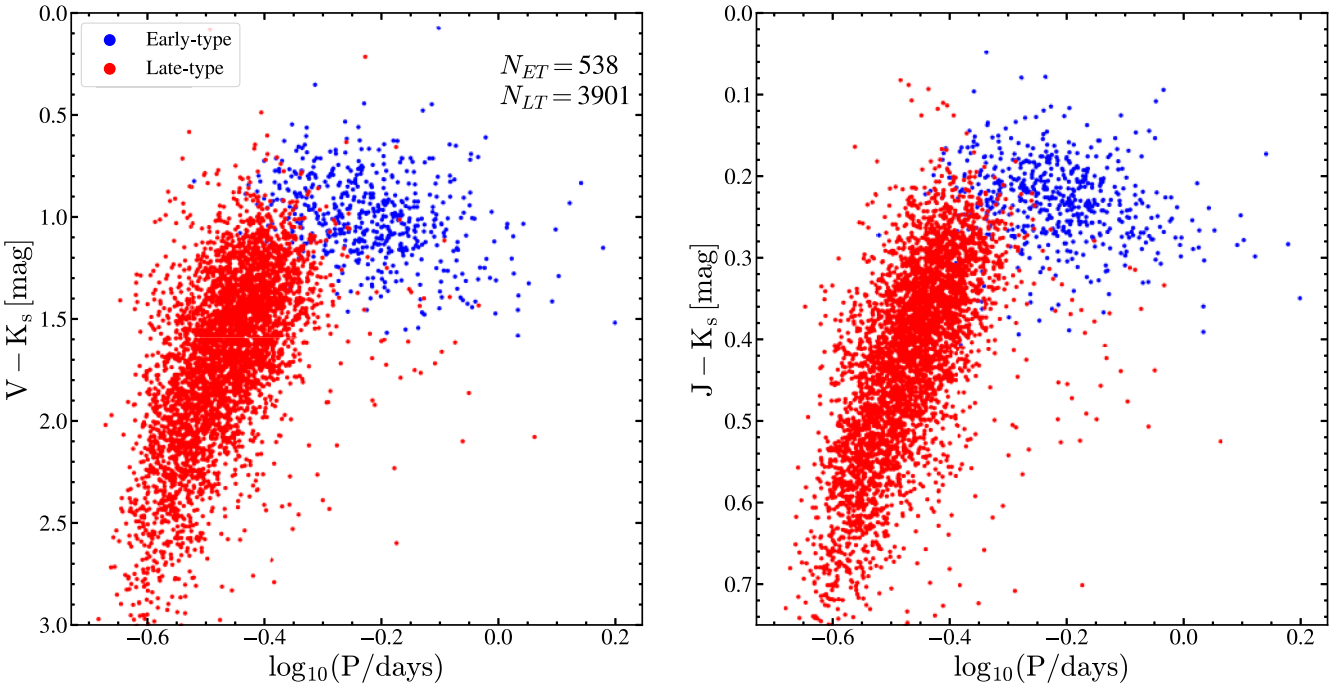

Figure 9. $V-K_{\rm s}$ (left-hand panel) and $J-K_{\rm s}$ (right-hand panel) versus $\log(P/{\rm d})$ for the spectroscopically separated late-type (red) and early-type (blue) EW binaries separated in period–temperature space using equation (2), with Prob > 0.9 and $A_V < 0.5$ mag.

and late-type systems with spectroscopic information. To separate these systems based only on their orbital period, we use the cutoff of $\log(P/{\rm d}) = -0.30$ at the minimum of the period distribution in Fig. 5. We chose the cut based on the orbital period distribution of the ∼71 200 EW binaries in ASAS-SN, instead of deriving a different cut from Fig. 13 because it could be biased by selection effects in the spectroscopic sample. The usual cut of $\log(P/{\rm d}) = -0.25$ excludes a significant number of shorter period, early-type systems, but it does provide a clean sample of longer period, early-type systems. The best-fitting parameters, their uncertainties, the dispersion, and the number of sources used in the fit are listed in Tables 1 (late type) and 2 (early type) for the EW binaries separated in the period–temperature space, and in Tables 3 (late type) and 4 (early type) for the EW binaries separated by period.

Fig. 14 illustrates the PLRs of the late-type and early-type systems separated in the period–temperature space. The PLR slopes are

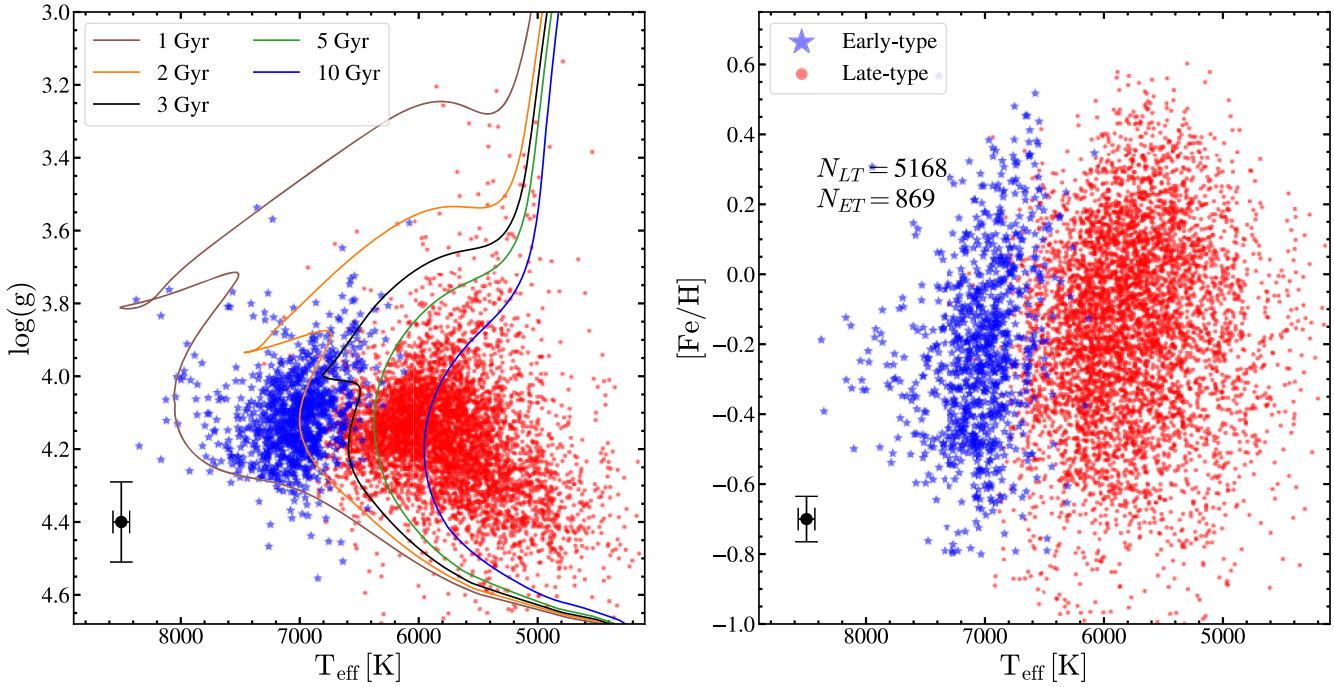

Figure 10. Distributions of the early-type and late-type contact binaries in log(g) versus $T_{\rm eff}$ (left-hand panel) and $T_{\rm eff}$ versus [Fe/H] (right-hand panel). MIST isochrones (Choi et al. 2016; Dotter 2016) for single stars with [Fe/H] = −0.25 at 1, 2, 3, 5, and 10 Gyr are shown for comparison. The average uncertainties are shown by the black error bars.

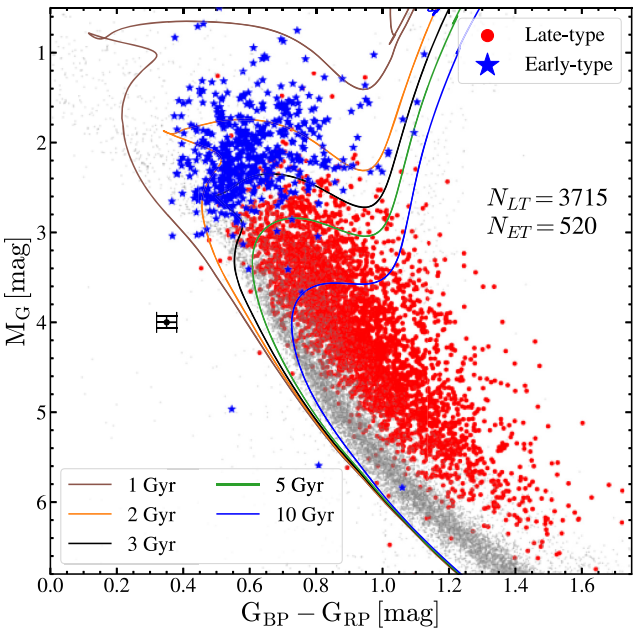

Figure 11. *Gaia* DR2 CMD for a sample of the early-type (blue) and late-type (red) EW binaries with Prob > 0.90, $A_V < 1$ mag, and parallaxes better than 10 per cent, which were separated in the period–temperature space using equation (2). A sample of nearby sources with good parallaxes and photometry is shown in grey. MIST isochrones (Choi et al. 2016; Dotter 2016) for single stars with [Fe/H] = −0.25 at 1, 2, 3, 5, and 10 Gyr are shown for comparison. The average uncertainties are shown by the black error bars. Solar-metallicity MIST isochrones lie on the grey points.

significantly different for the early-type and late-type binaries. The PLR slopes for the late-type systems separated in the period–temperature space also differ by $\lesssim$1 per cent from the PLR slopes of the late-type systems separated by period. The slopes for the late-type systems derived with these two samples are consistent, given the errors. On the other hand, early-type systems have slopes that differ by ∼1 per cent in the V band and ∼25 per cent in the K_s band. The near-infrared (NIR) PLR slopes for the early-type systems between the two ways of separating the EW sub-types are inconsistent, given their uncertainties. The slopes of the PLR fits for the late-type binaries differ by $>3\sigma$ from those obtained by Chen et al. (2018), but the disagreement is smaller for the NIR PLRs. For example, their V-band (-9.14 ± 0.40) and K_s-band (-5.95 ± 0.21) slopes are shallower than the slopes derived here by ∼14 and ∼7 per cent, respectively. In addition, at the median period $P \sim 0.34$ d of the late-type EW binaries, the PLR fits differ by ∼0.3 mag in the V band and ∼0.1 mag in the K_s band from those obtained by Chen et al. (2018). These differences are smaller than the scatter in the PLRs at these bands. Chen et al. (2018) derived PLRs for the late-type contact binaries based on a small sample of only 183 nearby ($d < 330$ pc) sources with an average extinction of $A_V = 0.075 \pm 0.025$ mag, whereas our PLR fits are made to a much bigger sample (∼61 times) across a wider range in distance and A_V. There are no significant changes in the PLR fits if we restrict our sample to smaller extinctions ($A_V < 0.5$ mag). Contact binaries are more diverse and span a much larger range in luminosity and temperature than classical pulsators like RR Lyrae and Cepheids, leading to more dispersion about the PLR.

5 CONCLUSIONS

We analysed a sample of 71 242 W UMa EBs, including 12 584 new discoveries, in the ASAS-SN V-band catalogue of variable stars,

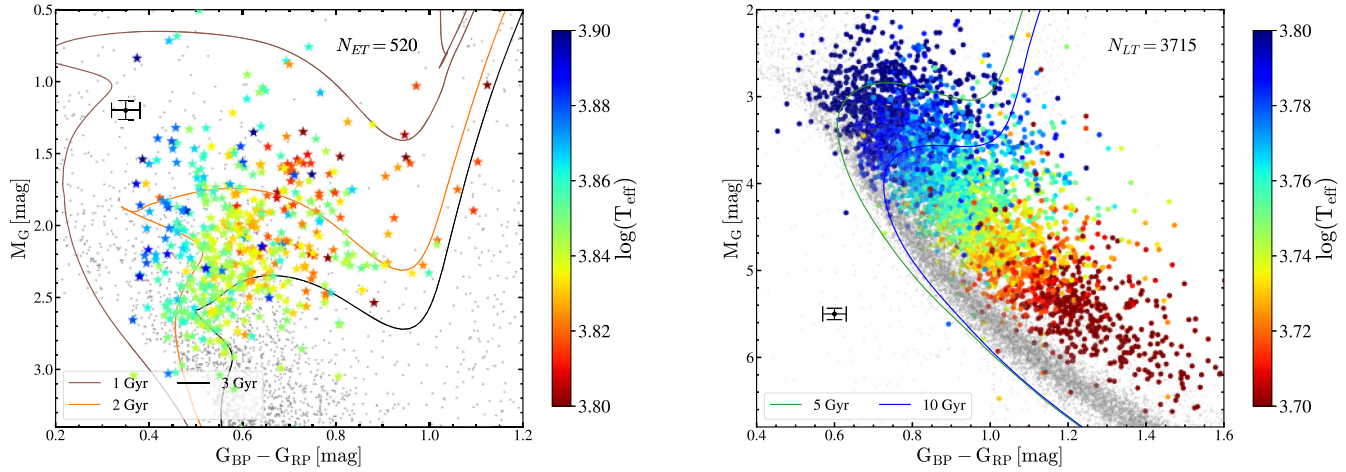

Figure 12. *Gaia* DR2 CMDs for the early-type (left-hand panel) and late-type (right-hand panel) EW binaries shown in Fig. 11, coloured by log ($T_{\rm eff}$). The colour bars show the same dynamic range in log ($T_{\rm eff}$) of 0.1 dex. A sample of nearby sources with good parallaxes and photometry is shown in grey. MIST isochrones (Choi et al. 2016; Dotter 2016) for single stars with [Fe/H] = −0.25 at 1, 2, 3, 5, and 10 Gyr are shown for comparison. The average uncertainties are shown by the black error bars.

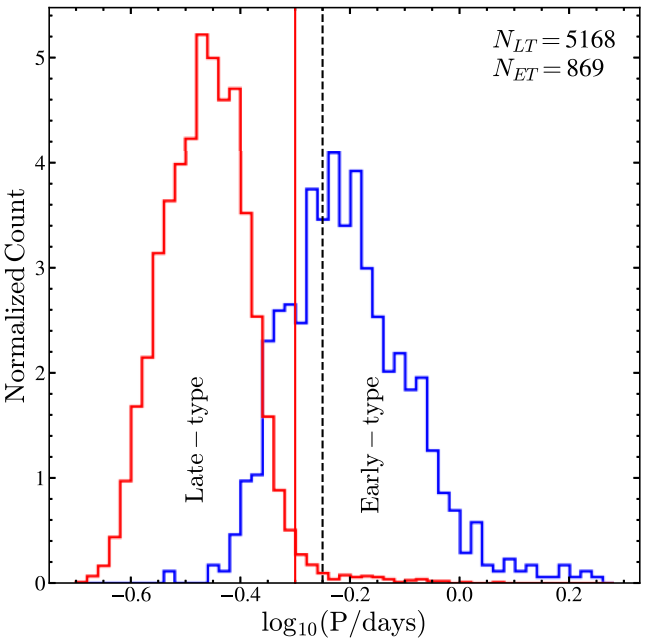

Figure 13. The distribution of orbital periods for the early-type (blue) and late-type (red) EW binaries that were separated in the period–temperature space using equation (2). The usual period cut separating early-type and late-type systems of $\log(P/{\rm d}) = -0.25$ is shown as a dashed black line. The suggested period cut of $\log(P/{\rm d}) = -0.30$ for separating the systems is shown as a solid red line.

taking advantage of their *Gaia* DR2 parallaxes (Gaia Collaboration et al. 2018a) and the spectroscopic temperatures, metallicities, and log(g) estimates from primarily LAMOST, but also GALAH, RAVE, and APOGEE, for 7169 of the stars. The large sample size and (in particular) the spectroscopic temperatures lead to a much clearer view of the dichotomy between early- and late-type systems. The period distribution has a clear minimum at $\log(P/{\rm d}) = -0.30$, making it a better separator between the two populations than the standard of $\log(P/{\rm d}) = -0.25$. The PLR also has a distinct break in its slope at the same period.

Table 1. PLR parameters for the late-type contact binaries separated in the period–temperature space.

Band	A (mag)	B (mag)	σ (mag)	N
W_{JK}	− 5.527 ± 0.052	1.469 ± 0.049	0.197	11 384
V	− 10.628 ± 0.052	2.360 ± 0.054	0.383	11 134
G	− 10.173 ± 0.047	2.379 ± 0.050	0.337	11 329
J	− 7.651 ± 0.049	1.763 ± 0.054	0.254	11 363
H	− 6.589 ± 0.047	1.623 ± 0.048	0.222	11 414
$K_{\rm s}$	− 6.381 ± 0.051	1.601 ± 0.045	0.214	11 387
W_1	− 6.369 ± 0.051	1.540 ± 0.051	0.199	11 579

Table 2. PLR parameters for the early-type contact binaries separated in the period–temperature space.

Band	A (mag)	B (mag)	σ (mag)	N
W_{JK}	− 3.616 ± 0.048	1.499 ± 0.049	0.140	226
V	− 2.770 ± 0.049	2.407 ± 0.051	0.166	221
G	− 2.977 ± 0.047	2.426 ± 0.049	0.154	228
J	− 3.512 ± 0.050	1.799 ± 0.049	0.144	226
H	− 3.535 ± 0.050	1.650 ± 0.050	0.145	231
$K_{\rm s}$	− 3.520 ± 0.051	1.612 ± 0.043	0.142	228
W_1	− 3.565 ± 0.056	1.583 ± 0.045	0.129	234

Table 3. PLR parameters for the late-type contact binaries separated by period.

Band	A (mag)	B (mag)	σ (mag)	N
W_{JK}	− 5.523 ± 0.049	1.482 ± 0.059	0.195	11 118
V	− 10.531 ± 0.047	2.373 ± 0.047	0.378	10 843
G	− 10.076 ± 0.047	2.410 ± 0.057	0.331	11 007
J	− 7.678 ± 0.046	1.753 ± 0.051	0.251	11 089
H	− 6.612 ± 0.048	1.619 ± 0.054	0.220	11 148
$K_{\rm s}$	− 6.402 ± 0.044	1.581 ± 0.053	0.212	11 123
W_1	− 6.359 ± 0.055	1.545 ± 0.055	0.197	11 300

Table 4. PLR parameters for the early-type contact binaries separated by period.

Band	A (mag)	B (mag)	σ (mag)	N
W_{JK}	-2.640 ± 0.051	1.403 ± 0.059	0.258	1199
V	-2.753 ± 0.049	2.328 ± 0.047	0.351	1176
G	-2.772 ± 0.049	2.379 ± 0.051	0.334	1186
J	-2.635 ± 0.051	1.716 ± 0.050	0.284	1189
H	-2.675 ± 0.048	1.575 ± 0.053	0.271	1198
K_s	-2.656 ± 0.051	1.528 ± 0.054	0.269	1203
W_1	-2.709 ± 0.055	1.487 ± 0.060	0.250	1192

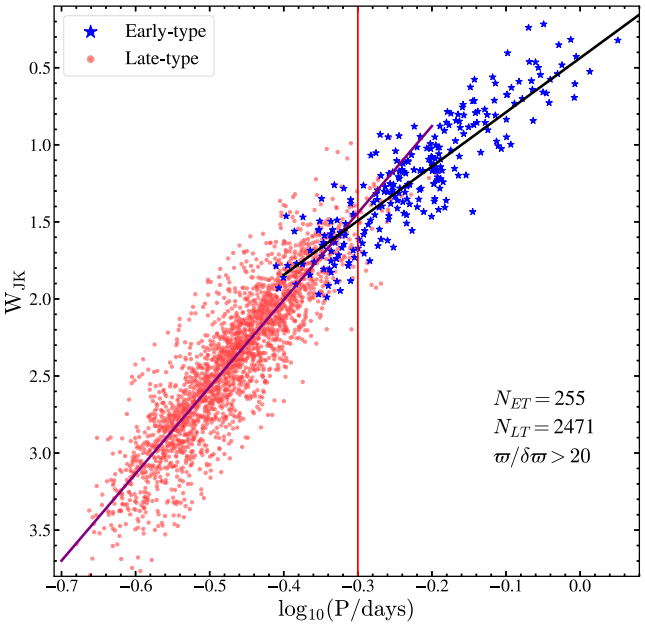

Figure 14. The Wesenheit W_{JK} PLR diagram for the EW stars separated in the period–temperature space using equation (2), with Prob > 0.98, $A_V < 1$ mag, and parallaxes better than 5 per cent after clipping outliers with dispersions $>3\sigma_r$ from the respective PLR fit. The fitted PLRs for the late-type and early-type contact binaries are shown as purple and black lines, respectively. The suggested period cut of $\log(P/\mathrm{d}) = -0.30$ for separating the systems is shown as a solid red line.

The distinction between the populations is even clearer in the space of period and effective temperature, where there is essentially a gap along the line $T_{\rm eff} = 6710\,\mathrm{K} - 1760\,\mathrm{K}\,\log(P/0.5\,\mathrm{d})$. There are neither strong distinctions between the populations in metallicity or $\log(g)$ nor strong correlations within the populations with these properties. Early-type systems are hotter at shorter orbital periods and get cooler as the orbital period increases. The total mass of the EW binaries increases with their orbital period. Thus, more massive early-type EWs are cooler and likely more evolved than the less massive early-type EWs that are hotter.

With the larger number of systems and a clearer separation of the two classes, we then derive revised PLRs for the late-type and early-type EW binaries in the W_{JK}, V, *Gaia* DR2 G, J, H, K_s, and W_1 bands for contact binaries both separated spectroscopically and by period. The slopes of the late-type PLRs for the two ways of dividing the systems were consistent with each other, given the uncertainties, but the slopes of the early-type PLRs differ by $\sim$25 per cent in the NIR. The slopes we find for late-type PLRs differ significantly ($\sim$10 per cent) from the existing PLRs for late-type EW binaries, given their uncertainties. This is likely due to the far smaller samples used by previous studies to derive PLRs.

The Kraft break appears to determine the observed dichotomy of the contact binaries. Stars lose angular momentum inefficiently above the Kraft break, making it unlikely that angular momentum loss is sufficient to bring the early-type systems into contact. Thus, early-type systems form due to stellar evolution and the subsequent expansion of a more massive component that is above the Kraft break ($\sim$1.3 $\mathrm{M}_\odot$). For the late-type systems, the primary is below the Kraft break, and the late-type systems can come into contact due to efficient angular momentum loss during the detached phase. The positions of the EW binaries on a *Gaia* DR2 CMD are consistent with early-type EW binaries being younger and more evolved than the late-type systems. Late-type EW binaries appear to be main-sequence binaries and the vast majority of these appear older than 5 Gyr. This is consistent with standard models for the formation and evolution of these systems (Jiang et al. 2014; Yildiz 2014).

ACKNOWLEDGEMENTS

We thank the referee, Dr. Diana Kjurkchieva, for the very useful comments that improved our presentation of this work. We thank Dr. Jennifer Johnson for useful discussions on this manuscript. We thank Las Cumbres Observatory and its staff for its continuing support of the ASAS-SN project. We also thank the Ohio State University College of Arts and Sciences Technology Services for helping us set up and maintain the ASAS-SN variable stars and photometry data bases.

ASAS-SN is supported by the Gordon and Betty Moore Foundation through grant GBMF5490 to the Ohio State University, and NSF grants AST-1515927 and AST-1908570. Development of ASAS-SN has been supported by NSF grant AST-0908816, the Mt. Cuba Astronomical Foundation, the Center for Cosmology and AstroParticle Physics at the Ohio State University, the Chinese Academy of Sciences South America Center for Astronomy (CASSACA), the Villum Foundation, and George Skestos.

KZS and CSK are supported by NSF grants AST-1515927, AST-1814440, and AST-1908570. BJS is supported by NSF grants AST-1908952, AST-1920392, and AST-1911074. TAT acknowledges support from a Simons Foundation Fellowship and an IBM Einstein Fellowship by the Institute for Advanced Study, Princeton. Support for JLP is provided in part by the Ministry of Economy, Development, and Tourism's Millennium Science Initiative through grant IC120009, awarded to The Millennium Institute of Astrophysics, MAS. Support for MP and OP has been provided by INTER-EXCELLENCE grant LTAUSA18093 from the Czech Ministry of Education, Youth, and Sports. The research of OP has also been supported by Horizon 2020 ERC Starting Grant 'Cat-In-hAT' (grant agreement no. 803158) and PRIMUS/SCI/17 award from Charles University. This work was partly supported by NSFC 11721303.

This work has made use of data from the European Space Agency (ESA) mission *Gaia* (https://www.cosmos.esa.int/gaia), processed by the *Gaia* Data Processing and Analysis Consortium. This publication makes use of data products from the Two-Micron All-Sky Survey, as well as data products from the *Wide-field Infrared Survey Explorer*. This research was also made possible through the use of the AAVSO Photometric All-Sky Survey, funded by the Robert Martin Ayers Sciences Fund.

This research has made use of the VizieR catalogue access tool, CDS, Strasbourg, France. This research also made use of ASTROPY, a community-developed core PYTHON package for astronomy (Astropy Collaboration et al. 2013).

REFERENCES

Alard C., 2000, A&AS, 144, 363
Alard C., Lupton R. H., 1998, ApJ, 503, 325
Alcock C. et al., 1997, ApJ, 486, 697
Andronov N., Pinsonneault M. H., Terndrup D. M., 2006, ApJ, 646, 1160
Astropy Collaboration et al., 2013, A&A, 558, A33
Bailer-Jones C. A. L., Rybizki J., Fouesneau M., Mantelet G., Andrae R., 2018, AJ, 156, 58
Bhatti W. et al., 2018, astrobase, v0.3.8, Zenodo. Available at: http://doi.org/10.5281/zenodo.1185231
Binnendijk L., 1970, Vistas Astron., 12, 217
Buder S. et al., 2018, MNRAS, 478, 4513
Cardelli J. A., Clayton G. C., Mathis J. S., 1989, ApJ, 345, 245
Casey A. R. et al., 2017, ApJ, 840, 59
Chen X., Han Z., 2009, MNRAS, 395, 1822
Chen X., de Grijs R., Deng L., 2016, ApJ, 832, 138
Chen X. et al., 2018, ApJ, 859, 140
Choi J. et al., 2016, ApJ, 823, 102
Cui X.-Q. et al., 2012, Res. Astron. Astrophys., 12, 1197
Cutri R. M. et al., 2013, VizieR Online Data Catalog, 2328
de Mink S. E. et al., 2013, ApJ, 764, 166
De Silva G. M. et al., 2015, MNRAS, 449, 2604
Derue F. et al., 2002, A&A, 389, 149
Dotter A., 2016, ApJS, 222, 8
Drake A. J. et al., 2014, ApJS, 213, 9
Eggen O. J., 1961, R. Greenwich Obs. Bull., 31, 101
Eggen O. J., 1967, Mem. RAS., 70, 111
Eggleton P. P., 1983, ApJ, 268, 368
Eggleton P. P., 2010, New Astron. Rev., 54, 45
Eggleton P. P., Kiseleva-Eggleton L., 2001, ApJ, 562, 1012
Eker Z. S. et al., 2006, MNRAS, 373, 1483
El-Badry K. et al., 2018, MNRAS, 476, 528
Flannery B. P., 1976, ApJ, 205, 217
Foreman-Mackey D . et al., 2013, PASP, 125, 306
Gaia Collaboration et al., 2018a, A&A, 616, 22
Gazeas K., Stępień K., 2008, MNRAS, 390, 1577
Graczyk D. et al., 2011, Acta Astron., 61, 103
Heinze A. N. et al., 2018, AJ, 156, 49
Henden A. A., Levine S., Terrell D., Welch D. L., 2015, AAS Meeting Abstracts
Holtzman J. A. et al., 2015, AJ, 150, 148
Jayasinghe T. et al., 2018, MNRAS, 477, 3145
Jayasinghe T. et al., 2019a, MNRAS, 486, 1907
Jayasinghe T. et al., 2019b, MNRAS, 485, 961
Jayasinghe T. et al., 2019c, MNRAS, 489, 4705
Jayasinghe T. et al., 2019d, MNRAS, 491, 13
Jiang D., Han Z., Li L., 2014, MNRAS, 438, 859
Kochanek C. S. et al., 2017, PASP, 129, 104502
Kovács G., Zucker S., Mazeh T., 2002, A&A, 391, 369
Kozai Y., 1962, AJ, 67, 591
Kraft R. P., 1967, ApJ, 150, 551
Lebzelter T. P. et al., 2018, A&A, 616, 8
Li L. et al., 2007, ApJ, 662, 596
Lidov M. L., 1962, Planet. Space Sci., 9, 719
Lucy L. B., 1976, ApJ, 205, 208
Madore B. F., 1982, ApJ, 253, 575
Majewski S. R. et al., 2017, AJ, 154, 94
Paczyński B. et al., 2006, MNRAS, 368, 1311
Pawlak M., 2016, MNRAS, 457, 4323
Pawlak M. et al., 2016, Acta Astron., 66, 421
Pojmanski G., 2002, Acta Astron., 52, 397
Qian S.-B. et al., 2017, Res. Astron. Astrophys., 17, 087
Royer F., Zorec J., Gómez A. E., 2007, A&A, 463, 671
Rucinski S. M., 1974, Acta Astron., 24, 119
Rucinski S. M., 1986, in Hearnshaw J. B., Cottrell P. L., eds, Proc. IAU Symp. 118, Instrumentation and Research Programmes for Small Telescopes, Kluwer, Dordrecht, p. 159
Rucinski S. M., 1994, PASP, 106, 462
Rucinski S. M., 1997, AJ, 113, 407
Rucinski S. M., 2006, MNRAS, 368, 1319
Samus N. N. et al., 2017, Astron. Rep., 61, 80
Scargle J. D., 1982, ApJ, 263, 835
Schlafly E. F., Finkbeiner D. P., 2011, ApJ, 737, 103
Schlegel D. J., Finkbeiner D. P., Davis M., 1998, ApJ, 500, 525
Shappee B. J. et al., 2014, ApJ, 788, 48
Skrutskie M. F. et al., 2006, AJ, 131, 1163
Taylor M. B., 2005 , in Shopbell P., Britton M., Ebert R., eds, ASP Conf. Ser. Vol. 347, Astronomical Data Analysis Software and Systems XIV, Astron. Soc. Pac., San Francisco, p. 29
Tonry J. L. et al., 2018a, PASP, 130, 064505
Tonry J. L. et al., 2018b, ApJ, 867, 105
Tylenda R. et al., 2011, A&A, 528, A114
Udalski A., 2003, Acta Astron., 53, 291
van Eyken J. C. et al., 2011, AJ, 142, 60
van Saders J. L., Pinsonneault M. H., 2013, ApJ, 776, 67
Vilhu O., 1982, A&A, 109, 17
Watson C. L., Henden A. A., Price A., 2006, Soc. Astron. Sci. Ann. Symp. 25, p. 49
Webbink R. F., 1976, ApJS, 32, 583
Webbink R. F., 2003, in Turcotte S., Keller S. C., Cavallo R. M., eds, ASP Conf. Ser. Vol. 293, 3D Stellar Evolution, Astron. Soc. Pac., San Fransicso, p. 76
Woźniak P. R. et al., 2004, AJ, 127, 2436
Wright E. L. et al., 2010, AJ, 140, 1868
Yakut K., Eggleton P. P., 2005, ApJ, 629, 1055
Yildiz M., 2014, MNRAS, 437, 185
Yildiz M., Doğan T., 2013, MNRAS, 430, 2029
Zechmeister M., Kürster M., 2009, A&A, 496, 577

This paper has been typeset from a TEX/LATEX file prepared by the author.